Engineering Structures 346 (2026) 121709

Contents lists available at ScienceDirect

Engineering Structures

journal homepage: www.elsevier.com/locate/engstruct

Deformation mode classification in extended endplate connections and implications on hysteretic response

Zizhou Ding, Ahmed Elkady *

Department of Civil, Maritime and Environmental Engineering, University of Southampton, Burgess Road, Boldrewood campus, Southampton SO16 7QF, United Kingdom

ARTICLE INFO

Keywords:
Extended endplate connection
Machine learning models
Damage mode classification
Finite element simulation
Hysteretic response

ABSTRACT

Determining the mode by which steel connections deform under rotational demands is essential for assessing damage, quantifying the associated losses, tuning design, and characterizing the connection's cyclic behavior. In this paper, a classification model is developed to predict the deformation mode in extended endplate connections (EEPCs) as a function of their layout, material, and geometric properties. The model covers six modes inclusive of those expected to occur in either fully rigid or partial strength EEPCs. Such modes, and particularly interactive ones, can be challenging to predict using traditional mechanical or analytical methods. The classification model utilizes the Random Forest algorithm and is trained using a large dataset of experimental and simulation data to achieve a high accuracy larger than 95 %. Additionally, recommendations are provided for characterizing hysteretic phenomenological models depending on the deformation mode. This includes an empirical formula for defining the cyclic pinching parameters in EEPCs undergoing endplate bending. This aims to support system-level seismic simulations employing the lumped plasticity approach.

1. Introduction

Extended endplate connections (EEPCs), shown in Fig. 1, are one of the popular steel connections in construction practice due to the ease of shop fabrication and on-site erection. These connections can be designed as fully rigid or partial strength connections to resist strong or moderate seismic loads. In either case, EEPCs are expected to develop appreciable moment resistance, ductile plastic deformation, and energy dissipation capacity. In that regard, the moment-rotation response and corresponding deformation mode(s) of EEPCs need to be studied towards efficient design, performance-based analysis, and repairability assessment of steel frames under different hazards (but primarily earthquakes). Fully rigid EEPCs are designed by current codes [1,2] to force the plastic deformation to occur in the beam. The backbone and hysteretic moment-rotation response of fully rigid EEPCs can be computed and simulated using available models [3,4]. For partial strength EEPCs, empirical models became recently available that capture the full range backbone moment-rotation response [5,6]. However, accurate models that predict the deformation mode(s) of partial strength EEPCs remain missing. Partial strength EEPCs can develop several deformation modes as observed in past experimental and numerical studies, including endplate bending, column flange bending, and column web/panel zone in shear. Beam yielding is also observed when the EEPC strength is close to the fully rigid boundary. Those deformation modes may occur individually or simultaneously depending on the connection's geometry and the relative strength of its components. This indicates that accurately predicting the deformation modes of EEPC can be challenging. Code-based methods, including the component method [2] and the yield line analysis [1,7] can be used to infer the deformation modes of EEPCs by identifying the weakest component. However, these models have practical limitations related to procedure complexity and prediction accuracy, particularly when dealing with multiple simultaneous deformation modes [8].

The deformation mode also controls the hysteretic moment-rotation behavior of the connection. In EEPCs, the hysteretic behavior can vary from a rounded response to a pinched one. The former is observed in fully rigid connections where beam local buckling is dominant while the latter is observed in partial strength connections controlled by plastic deformations in the connected plates (i.e., stiffness degradation and gap opening/closing between the endplate and column flange during the unloading and reloading process). A higher level of pinching reduces the seismic energy dissipation. The level of pinching depends on the deformation mode(s) and the connection geometry. Currently, there are no generalized recommendations for the definition of the cyclic

* Corresponding author.
E-mail addresses: zd3e20@soton.ac.uk (Z. Ding), a.elkady@soton.ac.uk (A. Elkady).

https://doi.org/10.1016/j.engstruct.2025.121709
Received 27 June 2025; Received in revised form 28 September 2025; Accepted 31 October 2025
Available online 3 November 2025

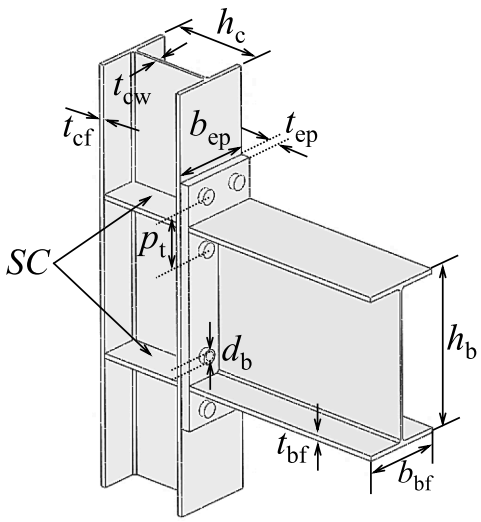

Fig. 1. EEPCs' general layout and key geometric parameters.

(pinching) parameters of EEPCs as part of existing numerical phenomenological models.

This paper aims to address these gaps by providing guidelines for capturing the cyclic response characteristics of EEPCs as a function of the dominant deformation mode. The paper is divided into two main parts. In the first part, several non-parametric machine learning models are employed to develop a deformation mode classification model. The models are trained using a large dataset with over 1500 specimens from past experimental research and new parametric continuum finite element simulations. In the second part, the cyclic response of EEPCs is assessed as a function of the deformation mode. A numerical phenomenological model is then calibrated with cyclic data. Recommendations are accordingly provided for the characterization of the cyclic deterioration parameters.

2. Description of primary deformation modes

Four primary deformation modes are identified in EEPCs as illustrated in Fig. 2. Those are endplate bending (EPB), column flange bending (CFB), column web-panel zone distortion in shear (CWS), and beam local buckling (BB). These modes may occur individually or simultaneously. This section provides a brief description of those modes including their deformation characteristics and applicability in design.

Beam local buckling (BB), shown Fig. 2(a), is the primary deformation mode in fully rigid EEPCs. This connection type is used in highly seismic regions, as part of pre-qualified EEPCs [9,10]. By definition, fully rigid EEPCs with BB develop a moment capacity larger than that of the beam's plastic moment ($M_{p,b}$) and can develop a rotational capacity larger than 4 % radian under cyclic loads. This mode results in excellent energy dissipation due to the rounded hysteretic response. On the other hand, the repairability of the BB mode (after earthquakes or column loss scenarios) can be challenging and costly.

In partial strength EEPCs, plastic deformations occur in the connection components such as endplate bending (EPB) and/or column flange bending (CFB). The controlling mode is dependent on the relative thickness of those two components. EPB (see Fig. 2(b)) occurs when a -relatively- thin endplate and strong bolts are implemented in design relative to the column flange (i.e., $t_{ep} << t_{cf}$). This can be achieved by designing the endplate to be the weakest component using the component method [2] or the yield line method [7]. EPB is a favorable mode that is sought in the design of partial strength EEPCs as it can achieve an acceptable energy dissipation capacity and plastic rotation over 3 % radian. Besides, the repairability of an endplate is simpler and more cost-effective compared to beam or column damage. On the other hand, EEPCs with an EPB mode possess a limited moment resistance (typically less than 80 % of $M_{p,b}$).

Column flange bending (CFB) can also occur in partial strength EEPCs (see Fig. 2(c)). CFB is not desirable in structural design since the columns are stipulated to remain elastic for structural stability. Additionally, the repairability of column plastic deformation can be problematic [11]. Nonetheless, CFB can still be observed particularly in unstiffened interior EEPCs undergoing column loss scenarios [12,13]. In this case, the column flanges are subjected to combined bending and tension from the catenary action.

Column web-panel zone distortion in shear (CWS), see Fig. 2(d), can occur in both fully rigid and partial strength EEPCs. Current design codes only allow for limited CWS deformations to prevent excessive drift and misalignment. Recently, considering the stable hysteretic response of the CWS mode, some researchers advocated for employing a weak panel zone design while providing detailing recommendations for limiting the weld fracture probability in case of welded connections [14]. CWS can develop a high energy dissipative capacity and strength hardening, which is critical for the seismic stability of moment resisting frames [15]. Like BB, the repairability of the CWS mode can be costly and challenging.

3. Dataset and data filtering

A large dataset, of 1546 specimens, is assembled to develop the classification model, which includes both experimental and simulated data. The dataset is concerned with bare steel beam-to-column joints with either fully rigid or partial strength/semi-rigid EEPCs. The dataset excludes EEPCs with endplate rib stiffeners or test specimens with rigid columns. The dataset includes the full geometric and material properties of the connections as well as the observed deformation mode(s). The experimental data comprises 265 specimens that are obtained from the digital database compiled by Ding and Elkady [8]. Parametric continuum finite element (CFE) simulations were conducted to complement the experimental dataset. A total of 1281 CFE simulations were conducted considering both American (wide flange) and European hot-rolled sections. All specimens were part of an external joint except

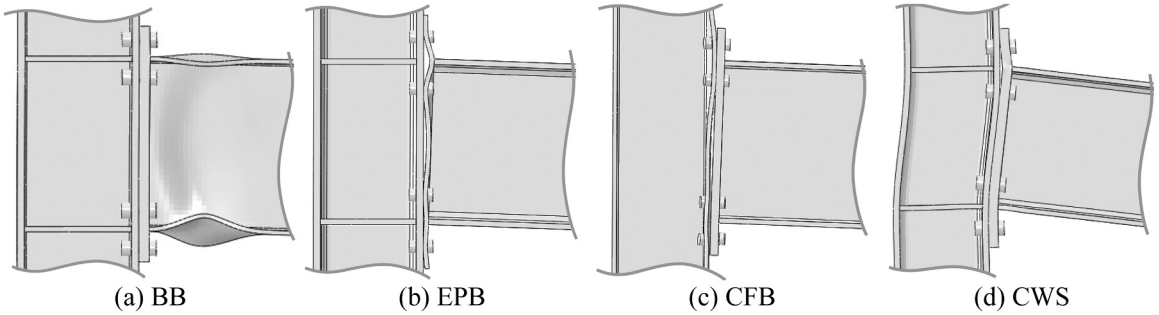

Fig. 2. EEPCs' primary deformation modes: (a) BB; (b) EPB; (c) CFB; (d) CWS.

Table 1
Summary of the geometric and material parameters used in the CFE simulations.

Column	Beam	Bolt	t_{ep} [mm]	Material grade	
				Bolt	Endplate
HEA 200–280 HEB 200–400 W310x33–360 × 634	IPE 300–600 W 310 × 74–920 × 238	M18 to M30 7/8" to 1–1/2"	10–40	8.8 10.9	S235 S275 S355

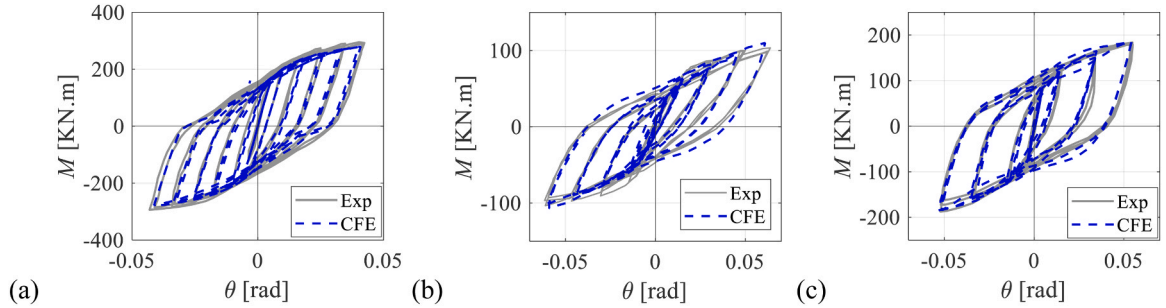

Fig. 3. Validation of the CFE model against cyclic data: (a) specimen *JD3* by [19]; (b) specimen *ESC* by [20]; (c) specimen *SE1* by [21].

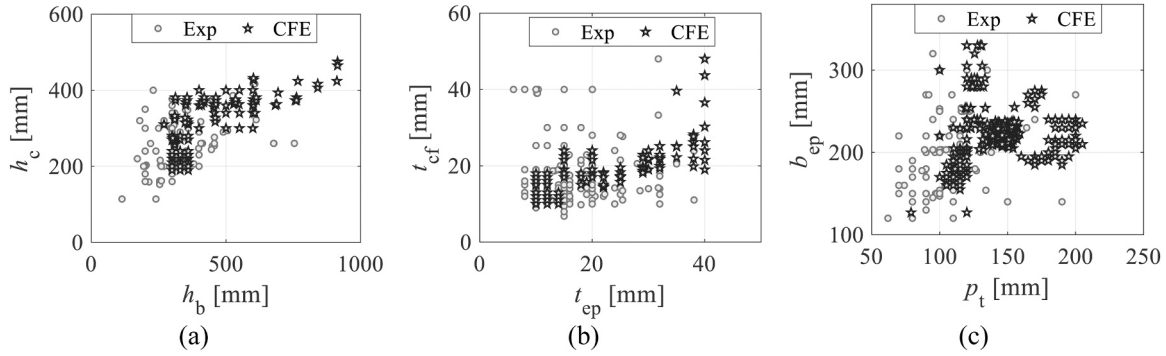

Fig. 4. Dataset design space distribution.

for 545 which were interior (cruciform) joints with symmetric load applied on the beams' ends. Table 1 summarizes the EEPCs' key geometrical and material parameters of the simulated specimens.

The specimen's response under monotonic loading is simulated in ABAQUS-FEA/CAE [16] using the standard static solver. The beam and column components are modeled using the linear brick element with incompatible modes *C3D8I* while the endplate was modeled using the quadratic brick element *C3D20R* with reduced integration. At least two mesh elements are generated across the flange thickness and the endplate thickness. A nonlinear material model with kinematic/isotropic hardening, which is based on the Von Mises yield criterion, is considered. The material basic parameters (i.e., elastic modulus and yield strength) are randomly sampled from pre-defined normal distributions. The cyclic hardening parameters recommended by [17] for mild steel are used. The column ends and the beam free end had pinned boundary conditions representing the moment inflection points. Both the column and the beam are allowed to move longitudinally (i.e., allowed to shorten axially). Welds are implicitly modeled using a "*Tie*" constraint. For the rest of the interacting components/surfaces, a general contact property is defined with a 0.3 coefficient of friction and "*penalty*" type normal interaction. Initial geometric imperfections are modeled in the beam by scaling and superimposing local buckling mode shapes as per the recommendation of [18]. Note that such imperfections are only critical for specimens that are expected to develop beam yielding or local buckling (i.e., those that develop BB or Balanced modes). Endplate geometric imperfections were not considered given that those might slightly affect the initial rotational stiffness of the connection but not its deformation mode. Selected specimens were simulated under ramped symmetric cyclic drifts, in relation to the second part of this paper. Fig. 3 shows sample validations against test specimens undergoing cyclic loading. Additional validations, demonstrating the deformation mode comparisons, are provided in the supplementary material. Essentially, the model can effectively capture the strength, stiffness, and pinching behavior of EEPCs. More details about the parametric data generation and additional validations of the CFE modeling approach can be found in Ding and Elkady [5].

Fig. 4 shows the design space covered by experimental and simulation data, with respect to key geometric parameters (refer to Fig. 1). The data uniformly covers all practical beam depths up to 900 mm (see Fig. 4(a)) and endplate thickness up to 40 mm (see Fig. 4(b)). Deeper beams with thicker endplates mostly correspond to fully rigid EEPC designs. Fig. 4(a) and (b) also demonstrate the expected proportionality between the beam and column sizes as well as the endplate and column flange thicknesses. Referring to Fig. 4(b), several specimens have a column flange thickness of over 40 mm. Those specimens were designed to have a strong column section developing no plastic deformation. The dataset also covers a wide range of the p_t parameter (the vertical pitch of the tension bolt rows) and the endplate width (see Fig. 4(c)). Finally, it is worth noting the consistent distribution of both the experimental and simulation data across the design space and the absence of data gaps.

The deformation mode(s) corresponding to each specimen in the dataset was deduced using a systematic method. For the experimental

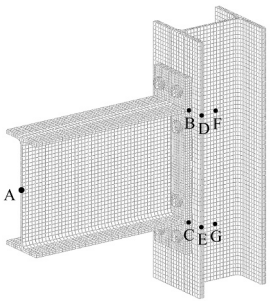

$$\theta_{total} = \frac{\delta_A}{L_b}$$

$$\theta_{pz} = \frac{\delta_F - \delta_G}{h_b}$$

$$\theta_{cf} = \frac{(\delta_D - \delta_E) - (\delta_F - \delta_G)}{h_b}$$

$$\theta_{ep} = \frac{(\delta_B - \delta_C) - (\delta_D - \delta_E) - (\delta_F - \delta_G)}{h_b}$$

$$\theta_b = \theta_{total} - \theta_{pz} - \theta_{cf} - \theta_{ep}$$

Fig. 5. Rotation contribution computation for the individual connection components.

data, the logged deformation modes were determined manually based on the specimen test photos and/or the damage mode description as reported by the different researchers in the literature. Several experimental studies involved thorough instrumentation and provided the rotation breakdown per connection component; making it easier to identify those that yielded. As previously noted, multiple modes may occur simultaneously. In this case, all these modes are logged. For the simulation data, the deformation mode(s) are numerically deduced based on the rotational contribution of each of the connection's components. Fig. 5 illustrates the equations used to deduce the individual rotational contributions from the CFE model. Those are based on the tracking of the displacement (δ) of several target points (points A to F). In this figure, δ_A refers to the vertical displacement at the beam end, and δ_B to δ_F refers to the horizontal displacement of each respective point. The rotational contribution of each component i is then expressed as a percentage of the total rotation (i.e., θ_i/θ_{total}). Any component contributing more than 20 % of the total rotation (evaluated at peak strength) is logged as a deformation mode. The 20 % threshold is deemed enough to capture components undergoing appreciable plastic deformation. Fig. 6 shows the rotation breakdown for three sample specimens and the corresponding -logged- deformation mode(s). In Fig. 6(a), the endplate (EPB) solely contributes more than 90 % of the total rotation. In Fig. 6 (b), both the endplate (EPB) and column flange (CFB) are deforming plastically while the beam remains elastic. In Fig. 6(c), EPB is the major mode, but it is accompanied by noticeable plasticity (> 20 % contribution) in the beam (BB) and column web (CWS).

For the classification model development, a total of six -deformation mode- classes were defined. Four of those involve the primary deformation modes defined earlier in Fig. 2(i.e., EPB, CFB, CWS, and BB) while two classes involve combined modes, namely, EPB+CFB and Balanced. Those two combined mode classes are included as they are frequently observed in practice. The Balanced mode refers to the occurrence of BB in addition to another one or more modes (most commonly BB+EPB, BB+CWS, and BB+EPB+CFB), as seen in Fig. 6(c). This Balanced class also represents a type of EEPCs that can develop the beam's plastic moment by balancing the plastic deformation between the beam and other components This EEPC type represents the boundary between fully rigid and partial-strength connections. Note that EEPCs experiencing BB+EPB are also referred to in the literature as an equal-strength joints [9,22].

Fig. 7 shows the distribution of the observed deformation mode classes for the entire dataset. The experimental dataset is largely focused on partial strength EEPCs; hence, the EPB, CFB, and EPB+CFB classes are the most observed. A smaller number of specimens involved fully rigid EEPCs with BB or Balanced classes. The simulation dataset also focused on partial strength EEPCs given that it is more challenging to predict the deformation mode(s) for such connections. In partial strength EEPCs, CWS is also observed, given that the column web panel zone is not necessarily designed for limited deformation as part of flexible framing construction in low to moderate seismicity.

4. Determination of significant predictors

Past studies concerned with predicting the parameters of EEPCs' moment-rotation response have established the key connection features that control their response [5,6]. The same features are employed herein for the prediction of the deformation mode. A total of 11 features are used that include geometric, material, and layout parameters. The geometric features (see Fig. 1) are the endplate thickness (t_{ep}), endplate width (b_{ep}), column flange thickness (t_{cf}), vertical bolt pitch distance (p_t), beam depth (h_b), beam flange slenderness (b_{bf}/t_{bf}), and column web slenderness (h_c/t_{cw}). The latter two are known to control BB and CWS, respectively. Fig. 8 shows the correlation of the deformation mode classes with some of the key geometric parameters. By visually inspecting Fig. 8(a), one can deduce that EEPCs mostly experience EPB when the t_{ep} is smaller than 15 mm and t_{ep}/t_{cf} is less than 1.0. This mode is also expected when p_t (i.e., the endplate bending length) is large relative to its thickness (i.e., p_t/t_{ep} larger than ~7 as deduced from Fig. 8 (b)). Similarly, CFB is likely to occur when t_{cf} is smaller than 15 mm, t_{ep}/t_{cf} is larger than 1.5, and p_t/t_{ep} is less than 7. The two modes are simultaneously observed (EPB+CFB) when the ratio of the two

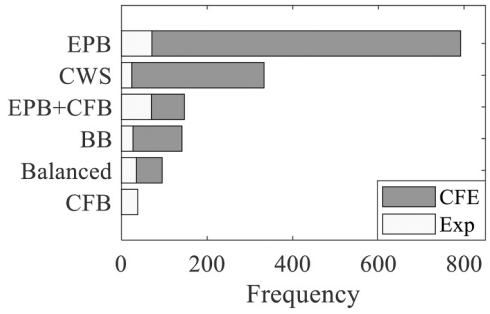

Fig. 7. Distribution of the observed deformation mode classes within the dataset.

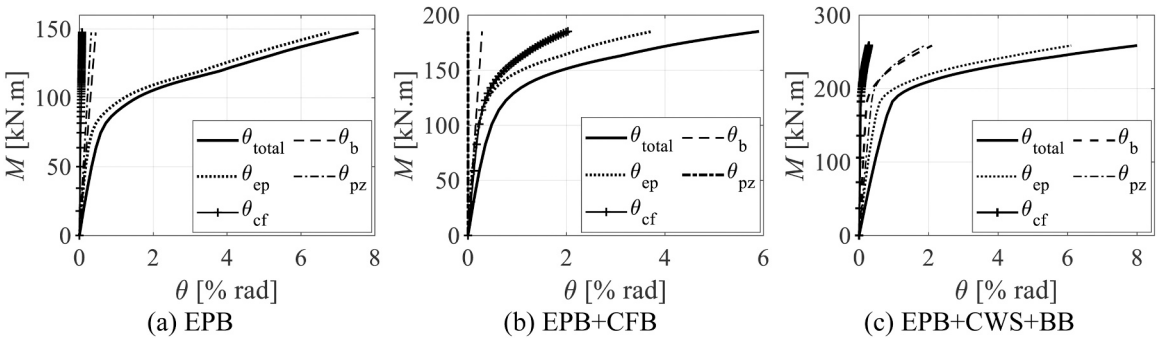

Fig. 6. Examples of the damage mode deduction from rotation contributions: (a) EPB; (b) EPB+CFB; (c) EPB+CWS+BB.

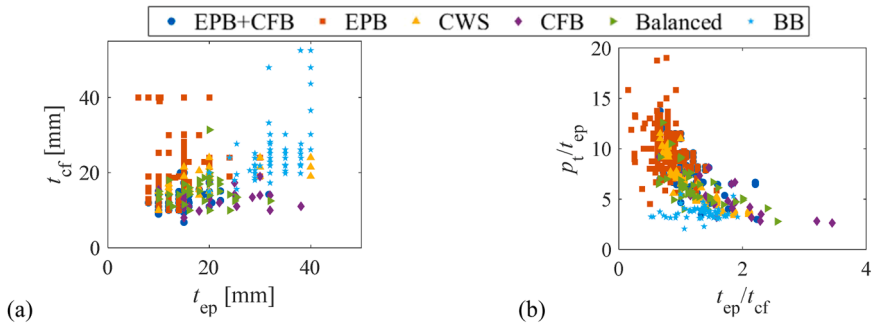

Fig. 8. Correlation between the deformation mode class and selected geometric features.

Table 2
Statistical summary of the numerical features [units: mm and MPa].

Parameters	*Joint*	*SC*	p_t	t_{ep}	t_{cf}	t_{cw}	h_c	h_b	b_{bf}	t_{bf}	b_{ep}	f_{yP}	f_{yC}
μ	0.38	0.52	127	19	19	12	292	417	186	14	204	344	382
σ	0.48	0.5	24	9	7	6	68	126	36	3	37	71	57
min	0	0	205	6	7	5	114	114	100	7	120	214	220
max	1	1	62	50	50	48	475	914	305	26	330	1022	1017

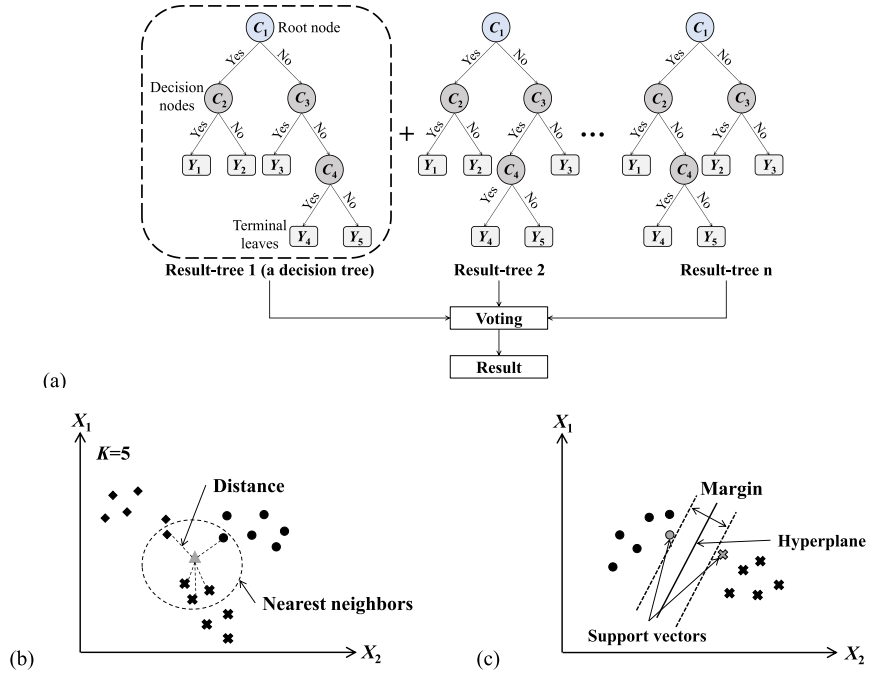

Fig. 9. Architecture of the classification models: (a) Tree-based; (b) KNN; (c) SVM.

thicknesses is close to unity. BB occurs in fully rigid EEPCs, which coincide with thick endplates (> 20 mm) and a p_t/t_{ep} value around 3.5. The latter is expected given the geometric limits specified for this type of seismically pre-qualified connections [9,23]. For the CWS and Balanced classes, deducing the classification boundary, based only on t_{ep}, t_{cf}, and p_t, is not simple since the latter mode can occur in a wide variety of connection layouts while the latter involves several deformation modes.

The two material features, endplate yield stress (f_{yP}) and column yield stress (f_{yC}), are considered as well. Those control the onset of yielding and the relative strength of the endplate and column flange components. Note that the beam's yield stress is not considered given that it was practically equal to that of the column, for the employed dataset. Finally, two layout features are considered: *SC* which reflects the presence of column flange stiffeners (continuity plates) given their role in restraining column flange bending. This feature is encoded by 0 and 1 for unstiffened and stiffened column specimens, respectively. Finally, the *Joint* type is considered to differentiate between external joints (or interior ones with asymmetric beam loading) and internal joints with symmetric beam loading. The former reflects the joint boundary conditions and load demands under lateral loading scenarios (e.g., earthquakes) while the latter reflects those under gravity loading scenarios (e.g., column loss/progressive collapse). This is important considering that CWS would be restricted in interior joints with symmetric loading at the beam ends. The *Joint* feature is encoded by 0 and 1 for exterior joints and interior joints with symmetric loading, respectively. The statistical summary of all features is shown in Table 2 to describe the design space covered by the dataset. The above features can be used, along with modern classification models, to better define the multi-dimensional boundary between the different deformation mode classes. These models are discussed in the next section.

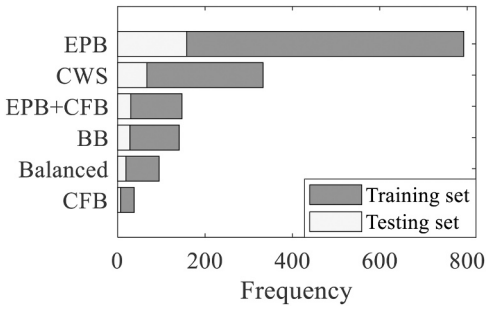

Fig. 10. Consistent distribution of the training and testing data sets.

5. Classification models' architecture and training

The dataset is used here to train some of the common machine-learning classification models. These are the Decision Tree (DT), Random Forest (RF), K-Nearest Neighbor (KNN), and Support Vector Machine (SVM). Fig. 9 illustrates the architecture of those models.

The architecture of a DT, as part of a RF, is illustrated in Fig. 9(a). The DT includes a roof node, decision nodes, and terminal leaves. The DT model starts by splitting the dataset from the root node using a defined condition (C_1) for a specific feature (X). The feature and the corresponding condition are determined based on an impurity algorithm; by default, Gini impurity [24]. This then branches into several decision nodes with other conditions (C_2 to C_n) for each of the remaining features until the impurity quantity is no longer reduced. The terminal leaves (Y_1 to Y_n) are the final predictions (i.e., classification), which can be tracked by following a branch from the root node. RF is an ensembled DTs (e.g., 100 DTs) with a Bagging algorithm [25]. For each DT, a bootstrapped dataset is selected for the training, and a subset of features (X) is selected for C_1 to C_n. The split of each tree follows an impurity algorithm, the same as the DT. The RF's final prediction is essentially the class with the voting majority based on the DTs' terminal leaves.

The KNN's architecture is illustrated in Fig. 9(b) using a 2-D example. Compared to tree-based models, KNN does not build an explicit model from the training data. Instead, the Euclidean distances (by default) between a testing data point and all other training data are computed. Then, all distances are sorted by an order, and the class of the nearest K points is determined as the prediction. Note that the number of K is recommended to be odd (3 by default) to avoid biased class voting.

The SVM's architecture is illustrated in Fig. 9(c) using a 2-D example. The SVM aims to split the data based on a plane (a straight line in a 2-D model) with the maximum margin. The maximum margin is an equal distance between the nearest points (i.e., support vectors) from different classes. For high-dimensional problems, the plane is no longer a line but a hyperplane. Therefore, the kernel trick function needs to be implemented to classify a nonlinear boundary. In this paper, the Radial Basis Function is selected for training.

All four classification models were developed using the MATLAB R2022a Classification Learner Toolbox [26]. The data was randomly split into 80 % and 20 % for the training and testing sets, respectively, while maintaining a consistent distribution between the two sets, as demonstrated in Fig. 10. For KNN and SVM, the data was normalized with the Z-score method, see Eq. (1), where X_i is feature i, $\overline{X}$ is the mean value of a feature, and σ is the standard deviation of a predictor. Note that data normalization is not required in tree-based models since 1) the split of each node is independently conducted, and 2) the threshold chosen for each split is consistent regardless of its scale.

$$X_{norm} = \frac{X_i - \overline{X}}{\sigma} \tag{1}$$

It can be observed from Fig. 7 and Fig. 10 that the number of specimens/observations for each deformation mode class is not consistent. This may induce bias in the classification model training algorithm and lead to poor predictive performance. In this regard, several methods can be implemented to alleviate this issue, such as the oversampling algorithm (i.e., SMOTE proposed by Chawla et al. [27]) for the minority class or assigning class weight factor [28]. A weighting factor is assigned herein, in pre-processing, for each deformation mode class within the training dataset, as summarized in Table 3. The weighing factors are computed as the inverse of the ratio of a given class's number of observations to the total number of observations divided by the number of classes [28]. This ensures the same importance level is given for each damage mode, which is a standard practice in classification model development.

Table 3
Weighting factors assigned to each deformation mode class.

Class	EPB	CWS	EPB+CFB	BB	Balanced	CFB
Weighting factor	0.33	0.78	1.76	1.82	2.71	6.65

6. Model performance

Fig. 11 shows the confusion matrices of the training and testing datasets for each of the four models. Three metrics are used to quantify the model performance: *accuracy* (A), *recall* (R), and *precision* (P). *Accuracy* measures the overall model's performance, which is the ratio of the correctly predicted specimens to the total number of specimens. *Recall* is the ratio of the correctly predicted specimens for a given class to the total number of specimens in the corresponding true class. *Precision* is the ratio of the correctly predicted specimens in a damage mode to the total specimens in the corresponding predicted class. Overall, all models achieve acceptable and consistent accuracy ($>$ 84 %) across both the training and testing datasets. The tree-based models, and the RF model in particular, show the highest performance with respect to all three metrics. The RF model predicts the testing dataset with an impressive 94 % accuracy. The recall and precision are over 90 % for EPB, BB, and CWS. Those classes have well-defined boundaries (refer to Fig. 8). Lower (but still acceptable $>$ 71 %) recall and precision values are noted for the CFB, Balanced, and EPB+CFB classes. This can be attributed to the lower number of specimens, material uncertainties, and the fact that the latter two classes involve combined deformation modes. Going forward, the RF model is selected for its superior performance.

To investigate the RF model's rationality from a mechanical perspective, the features' impurity-based importance indices are computed and plotted in Fig. 12(a). The impurity-based importance index is computed based on the feature that is used more frequently to split the data to reduce impurity. The figure shows the order of the features by their impurity-based importance. The geometric features t_{ep}, t_{cf}, and p_t are the top three features, accounting for about 50 % of the overall importance. This expected based on the earlier discussion (refer to Fig. 8) that demonstrated their strong correlation with the deformation mode class. The importance of h_c/t_{cw} is around 10 %. This is critical for the EEPC controlled by Balanced and CWS. The importance of f_{yP} and f_{yC} is around 8 % and 12 %, respectively. This is expected as those parameters are critical to control the endplate and column flange bending.

The importance of each feature relative to the deformation class is further investigated by computing the mean absolute SHAP values as shown in Fig. 12(b) which measures how much a given feature can impact the model predictions [29]. Similar to the impurity-based importance, t_{ep}, t_{cf}, and p_t are the top three features based on the aggregated SHAP importance values. The t_{ep} feature is the most influential for all classes, except for CFB and CFB+EPB that are more affected by t_{cf}. Note also that the feature *SC* shows a relatively higher importance, especially for EPB and EPB+CFB. This is because the column stiffening is critical to affect how much a column flange can deform.

The correlation of each feature with the predicted class probability (whether positive or negative) is investigated through the SHAP summary plots in Fig. 13. Referring to Fig. 13(a), t_{ep}, t_{cf}, and f_{yP} are positively

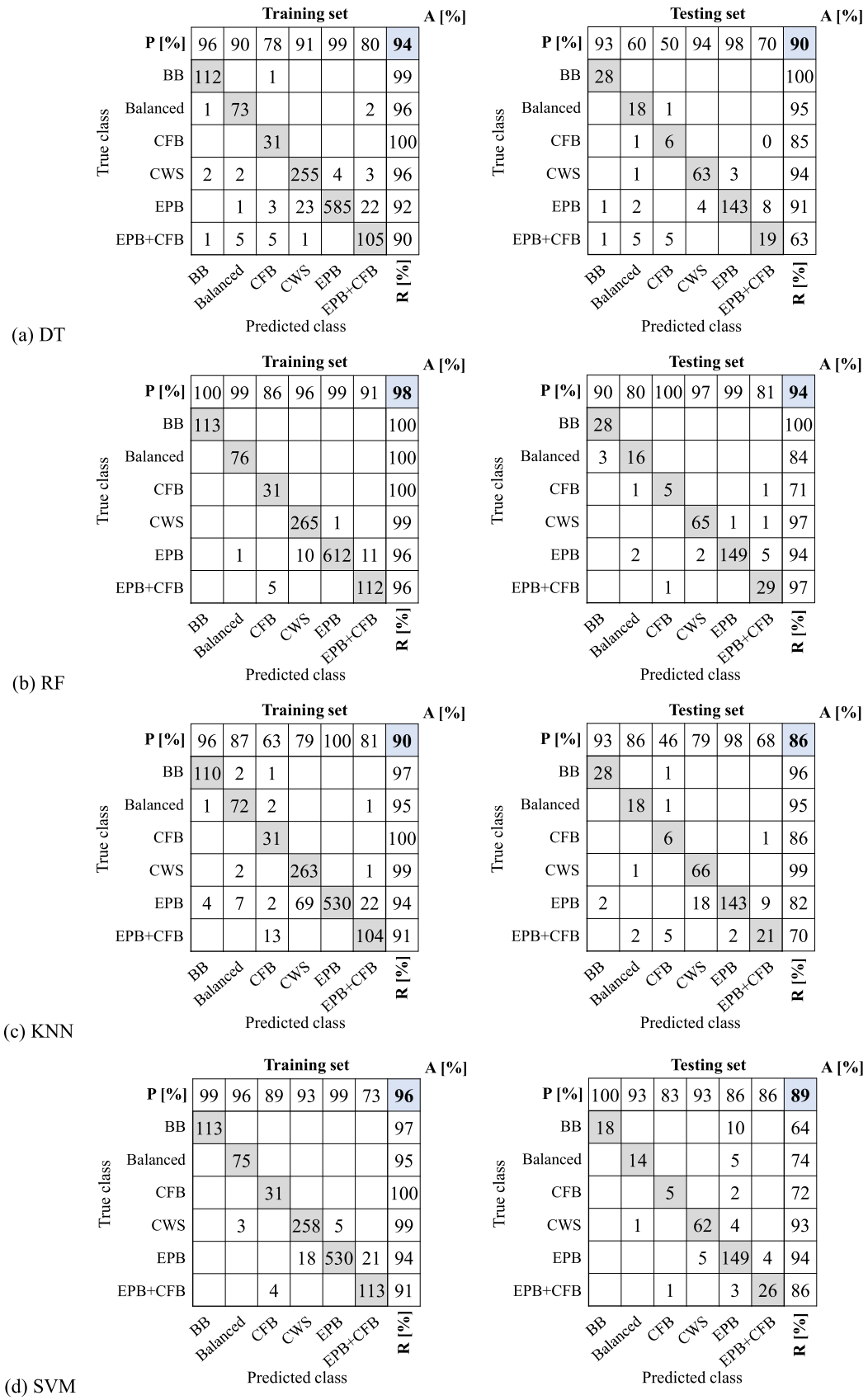

Fig. 11. Confusion matrices of the trained classification models: (a) DT; (b) RF; (c) KNN; (d) SVM.

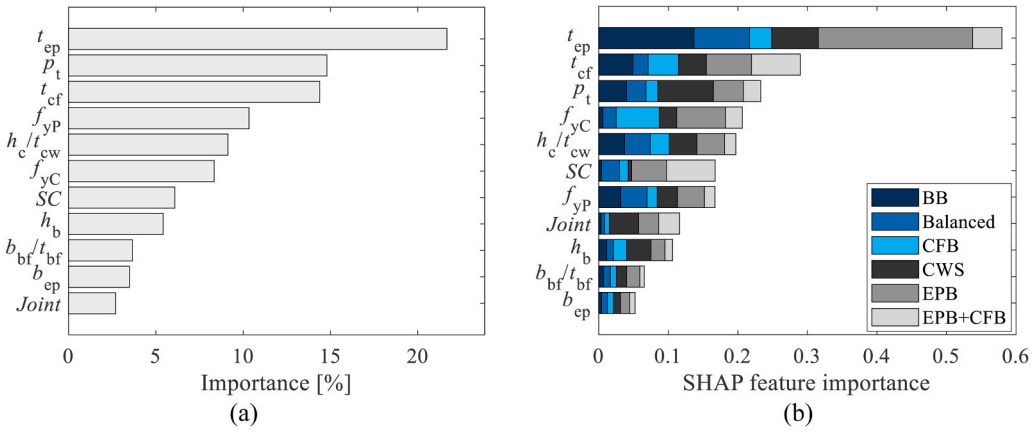

Fig. 12. Feature importance based on the RF model: (a) Impurity-based importance; (b) Mean absolute SHAP importance.

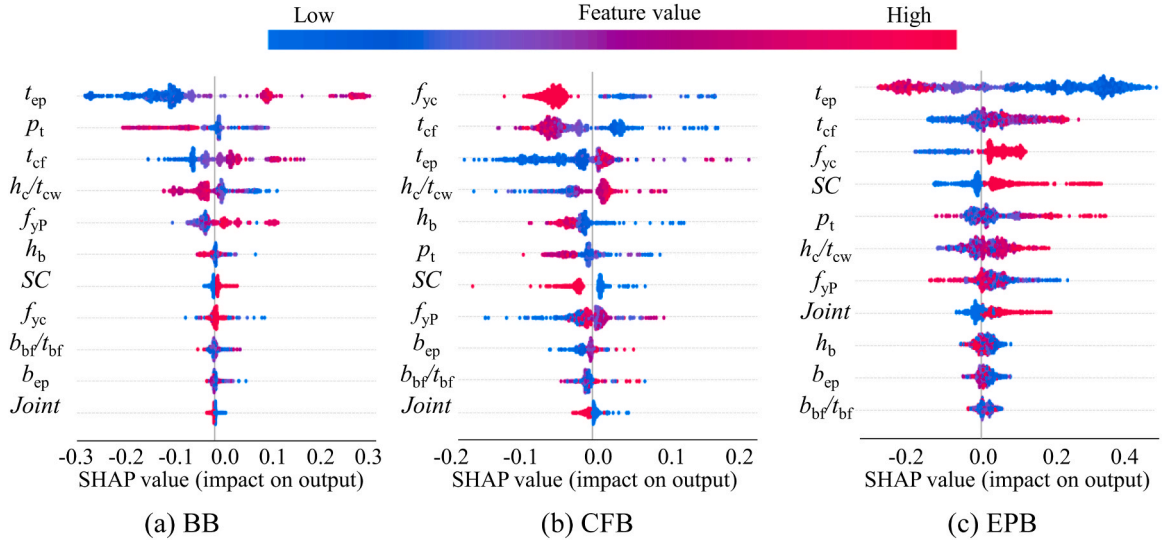

Fig. 13. SHAP value summary plots for the (a) BB, (b) CFB, and (c) EPB deformation modes.

correlated with the probability of predicting BB. This reflects the fact that when the connection components (i.e., column flange and endplate) are stronger, the beam is more likely to be the weak element. Similarly, a higher -encoded- *SC* value (i.e., stiffened column) will have a positive impact on BB likelihood. A smaller p_t is more likely to result in BB due to the restraint on endplate bending. This is also the case for deeper beams; primarily because fully rigid joints traditionally employ deep beams rather than shallow ones to control building drifts. Referring to Fig. 13 (b), except for t_{ep}, h_c/t_{cw}, and f_{yP}, all other features (especially, t_{cf} and f_{yC}) are inversely correlated with the CFB probability of occurrence, implying that either a stronger endplate or a weaker column flange would result in CFB. Opposite correlations are observed with respect to EPB as shown in Fig. 13(c). In summary, the employed model interpretation algorithms demonstrate model rationality and agreement with the established connection mechanics.

7. Implications on the hysteretic response

The EEPC deformation mode affects the characteristics of its hysteretic response. Knowing the hysteretic response dependency on the deformation mode is necessary when selecting and defining numerical hysteretic models as part of system-level simulations. This section investigates this dependency and provides guidelines for the definition of the cyclic parameters of existing phenomenological deterioration models within the *OpenSees* platform [30].

Concerning CWS, EEPCs produce a rounded hysteretic response with excellent energy dissipation, as shown in Fig. 14(a). The hysteretic behavior is stable without strength or stiffness degradation. Similarly, EEPCs developing BB produce a rounded hysteretic response, except that stiffness and strength degradation are triggered following the onset of local buckling (see Fig. 14(b)). As part of system-level simulations employing the lumped plasticity approach, the *hysteretic* material model (or an equivalent model) can be employed for CWS [31–33] while for BB, the *IMKBilin* phenomenological model [4] with a bilinear response can be used [3].

For EEPCs controlled by CFB, a peak-oriented hysteretic response is observed with a reduced re-loading stiffness due to the bending of the column flange (see Fig. 14(c)). The response can be captured by the *IMKPeakOriented* model while utilizing the backbone definition per the recommendations of Xu et al. [6] and Ding and Elkady [5]. For EPB, as observed in Fig. 14(d-f), EEPCs undergo a pinched behavior with reduced energy dissipation resulting from the gap opening/closing between the endplate and the column flange. The level of pinching depends on the connection's geometric parameters, particularly those controlling the endplate bending stiffness. This is investigated herein by calibrating the *IMKPinching* model against the hysteretic responses of 10 available test specimens plus 15 CFE simulations. Special attention is paid to the κ_f and κ_d parameters that control the onset of pinching in each

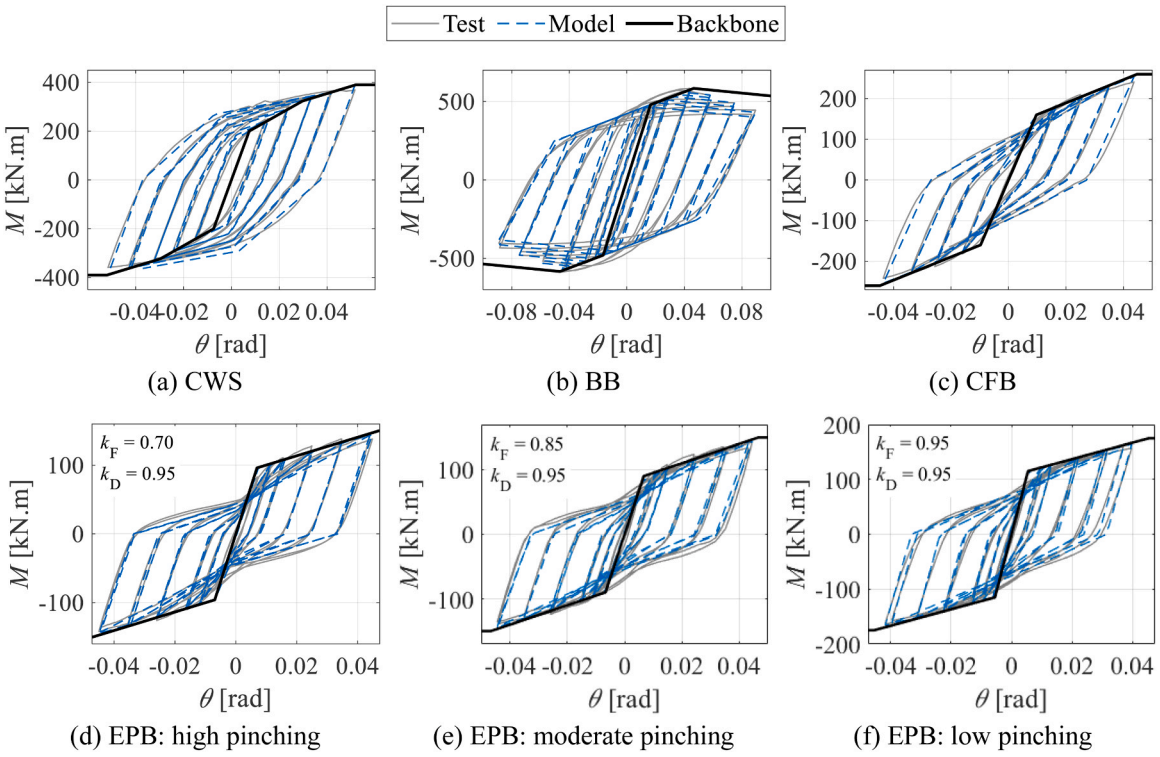

Fig. 14. Calibrated hysteristic responses for different deformation modes: (a) CWS; (b) BB; (c) CFB; (d) EPB: high pinching; (e) EPB: moderate pinching; (f) EPB: low pinching.

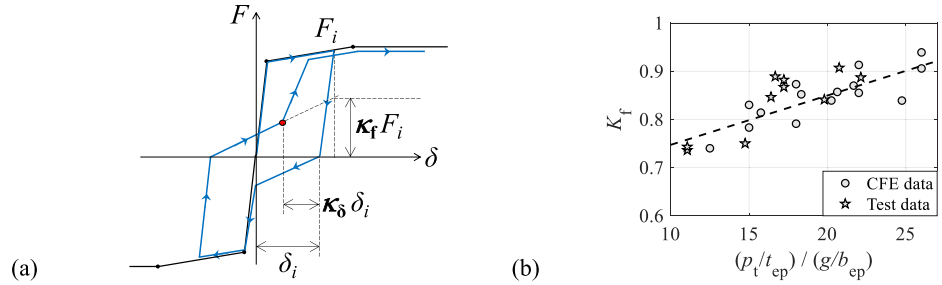

Fig. 15. (a) Definition of the pinching parameters; (b) correlation between κ_f and the endplate geometric parameters.

cycle (i.e., pinching level) with respect to the target force and deformation, respectively, as illustrated in Fig. 15(a).

Fig. 14(d-f) show three EPB hysteretic responses with varying pinching levels. High pinching levels are reflected by κ_f value as low as 0.7 (Fig. 14(d)) while low pinching levels are reflected by κ_f value as high as 0.95 (Fig. 14(f)). For κ_d, the value is almost constant as it varies between 0.95 and 1.0 (i.e., pinching starts near the zero-rotation position when the gap closes). Note that in all these simulations the reference hysteretic energy parameter (λ) was set as a large number since cyclic strength degradation does not occur in such connections. It was observed that κ_f correlates with the normalized geometric parameters p_t/t_{ep} (representing the plate bending stiffness in the vertical direction) and

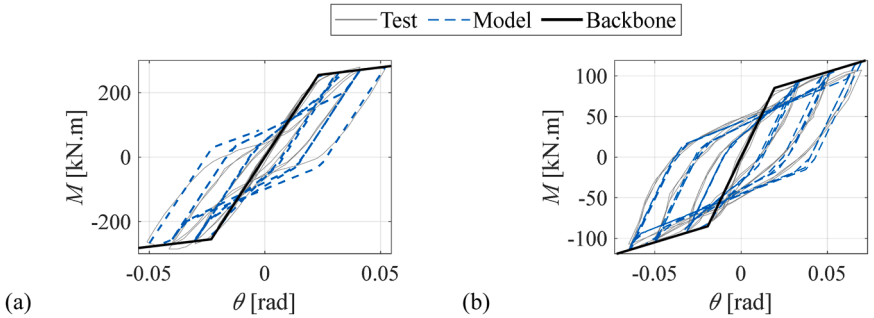

Fig. 16. Examples demonstrating the use of the predicted κ_f pinching parameter in generating hysteretic data: (a) Specimen *S2* by [34] $\kappa_f = 0.77$, and (b) specimen *ESC* by [20] $\kappa_f = 0.84$.

Table 4
Sample output of the classification model including class probability.

Exterior joint – Beam: IPE360 – Column: HEA300															
Example 1		*SC*	*Joint*		p_t	b_{ep}	t_{ep}/t_{cf}	h_b		h_c/t_{cw}		b_{bf}/t_{bf}	f_{yP}		f_{yC}
Standard	Input	0	0		120	220	12/14	360		290/9		170/13	385		385
	Output	BB		Balanced			CFB		CWS		**EPB**			EPB+CFB	
		0.01		0.03			0.0		0.18		**0.44**			0.33	
increasing t_{ep}	Input	0	0		120	220	18/14	360		290/9		170/13	385		385
	Output	BB		Balanced			CFB		CWS		EPB			**EPB+CFB**	
		0.01		0.1			0.07		0.13		0.06			**0.64**	
increasing t_{ep} and adding stiffeners	Input	1	0		120	220	18/14	360		290/9		170/13	385		385
	Output	BB		Balanced			CFB		**CWS**		EPB			EPB+CFB	
		0.04		0.15			0.07		**0.33**		0.19			0.22	
Exterior joint - Beam: W18x55 Column: W14x90															
Example 2		*SC*	*Joint*		p_t	b_{ep}	t_{ep}/t_{cf}	h_b		h_c/t_{cw}		b_{bf}/t_{bf}	f_{yP}		f_{yC}
Standard	Input	1	0		130	240	20/18	459		356/11		191/16	385		385
	Output	BB		Balanced			CFB		**CWS**		EPB			EPB+CFB	
		0.13		0.27			0.0		**0.37**		0.19			0.04	
Increasing t_{cw} by adding doubler plates	Input	1	0		130	240	20/18	459		356/22		191/16	385		385
	Output	BB		**Balanced**			CFB		CWS		EPB			EPB+CFB	
		0.17		**0.36**			0.02		0.21		0.21			0.03	
Increasing t_{ep}	Input	1	0		130	240	30/18	459		356/22		191/16	385		385
	Output	**BB**		Balanced			CFB		CWS		EPB			EPB+CFB	
		0.61		0.11			0.04		0.21		0.03			0.0	
Interior joint – Beam: UB 610x229x113 Column: UC 305x305x97															
Example 3		*SC*	*Joint*		p_t	b_{ep}	t_{ep}/t_{cf}	h_b		h_c/t_{cw}		b_{bf}/t_{bf}	f_{yP}		f_{yC}
Standard	Input	0	1		130	240	16/15	607		306/10		228/17	385		385
	Output	BB		Balanced			CFB		CWS		EPB			**EPB+CFB**	
		0.05		0.25			0.07		0.08		0.10			**0.44**	
		SC	*Joint*		p_t	b_{ep}	t_{ep}/t_{cf}	h_b		h_c/t_{cw}		b_{bf}/t_{bf}	f_{yP}		f_{yC}
Adding stiffeners	Input	1	1		130	240	16/15	607		306/10		228/17	385		385
	Output	BB		**Balanced**			CFB		CWS		EPB			EPB+CFB	
		0.05		**0.39**			0.04		0.17		0.27			0.08	
		SC	*Joint*		p_t	b_{ep}	t_{ep}/t_{cf}	h_b		h_c/t_{cw}		b_{bf}/t_{bf}	f_{yP}		f_{yC}
Increaseing t_{ep}	Input	1	1		130	240	32/15	607		306/10		228/17	385		385
	Output	**BB**		Balanced			CFB		CWS		EPB			EPB+CFB	
		0.43		0.19			0.07		0.20		0.08			0.03	

g/b_{ep} (representing the plate bending length in the horizontal direction). This is demonstrated in Fig. 15(b) based on the 25 test/CFE data points. A longer and thinner endplate (i.e., large p_t/t_{ep}) will result in lesser pinching while a higher bolt gauge with respect to the endplate width (g/b_{ep}) will result in higher pinching. Using linear regression, this relation can be represented by Eq. (2). This, in addition to the backbone parameters recommended by Ding and Elkady [5] and Xu et al. [6], completes the definition of the phenomenological model. The utilization of Eq. (2) to generate the appropriate hysteretic response is demonstrated in Fig. 16 against a couple of specimens with different levels of pinching. The figure demonstrates the validity of this model in capturing the overall response of the connections based on its geometric parameters.

$$\kappa_f = 0.80 + 0.023\frac{p_t}{t_{ep}} - 0.34\frac{g}{b_{ep}} \quad (2)$$

8. Model limitations

The proposed model has some limitations that could be further improved in the future. Those limitations are as follows:

- The developed RF model is only applicable to bare steel beam-to-column EEPCs. The applicability of the geometrical and material parameters shall be restricted to the ranges of the employed dataset (see Table 2). These ranges, however, should be sufficient to cover all practical design layouts.
- The model ignores any axial load exerted on the column and beam, due to the limited data available in the literature. Depending on its magnitude, the axial load can significantly affect the connection's deformation mode [35,36].
- EEPCs with rib plate stiffeners are not considered. However, given that rib stiffeners are typically used in fully rigid connections, the model herein can still be used to confirm the BB deformation mode. For other types of EEPCs, the current model may fall short considering that rib plate stiffener can restrain the endplate bending mechanism and even deform on its own [19,37].
- The used dataset assumes that the EEPC employs a strong bolt design. This means that the bolt is not a source of plastic deformation when the connection develops its plastic capacity. Therefore, specimens governed by a bolt elongation are not captured by the classification model. However, this type of connection is not one that is produced by standard design practice.
- The simulated dataset involved models that did not explicitly model the beam-to-endplate weld geometry. This might result in a slightly more flexible endplate in bending (i.e., larger predicted probability of EPB occurrence) compared to reality. This is truer for connections with large fillet-weld leg length and small p_t.
- The classification model assumes hot-rolled or built-up beam/column sections with non-slender flange/beam elements. The model also assumes the same material grade for the beam and the column. For the training dataset, the beam and column material grade are mostly A992 Gr. 50 or S355. Accordingly, the developed model cannot be used for joints employing slender (class 3) sections and may not be appropriate for those employing different member steel grades.

9. Practical implementation

The developed classification model is made available for users to assist in structural design and analysis. Considering that tree-based models cannot be simply presented in mathematical form, the model herein is provided in the form of a MATLAB function and through a graphical-user interface (GUI) tool; both of which are down able from GitHub [38]. In both cases, the user needs to specify the values of the *input* features (see Table 2). The function (or the developed GUI) will provide the *output* which is the predicted deformation mode class. Additionally, the *output* will display all the -six- deformation mode classes and their corresponding prediction probability in a descending order. The prediction probability is calculated as the ratio of the number of trees predicting a given class to the total number of trees. This information can help the user identify the confidence level in the predicted class and whether the prediction falls within an uncertain boundary between two or more classes. Table 4 shows few examples of the input and outputs of the MATLAB function. Note that all bolts in those examples are assumed as strong components. Example 1 is an unstiffened exterior joint with a shallow-depth beam ($h_b \leq 400$ mm) controlled by EPB, as the thin endplate is the weak component (i.e., $t_{ep} < t_{cf}$). By increasing t_{ep} from 12 mm to 18 mm, plastic deformations extend to the column flange (resulting in EPB+CFB). By further adding column stiffeners, the column flange deformation becomes restrained and plastic deformations are shifted to the column web, i.e., the joint becomes controlled by CWS.

Example 2. is a stiffened exterior joint with a medium-depth beam (400 mm$<h_b\leq$600 mm) controlled by CWS. By adding doubler plates, the column web becomes stiffer, and the plastic deformations move the endplate and beam flange (i.e., Balanced). If the t_{ep} is increased to 30 mm, the connected beam becomes the only weak component and BB domains the deformation mode (i.e., fully rigid joint).

Finally, Example 3 is an unstiffened interior joint with a deep beam (i.e., $h_b > 600$ mm) controlled by EPB+CFB as the t_{ep} and t_{cf} values are very close (i.e., $t_{ep}/t_{cf} \approx 1$). By adding column stiffeners to strengthen the column flange, plastic deformations dominate in the endplate (EPB). If t_{ep} is further increased to 30 mm, the joint will become rigid/full-strength, and BB controls its plastic deformations. These examples demonstrate that the proposed classification model can effectively and precisely capture the EEPCs' deformation modes with different configurations and geometric parameters.

10. Summary and conclusions

A classification model, based on the Random Forest algorithm, is developed to predict the deformation mode in EEPCs. Six deformation modes are considered covering both primary and interactive ones that are expected to occur in both fully rigid and partial strength EEPCs. The model was trained using a large dataset of carefully curated experimental and simulated data. The model prediction achieves a high overall accuracy (> 95 %) and can provide the prediction probability associated with each deformation mode. Further recommendations are provided regarding the numerical hysteretic models to be used for each deformation mode. Specifically, an empirical formula is developed to quantify the force-based pinching parameter (κ_f) as part of phenomenological *IMKPinching* model.

The developed model and recommendation are made available publicly through a MATLAB-based function and a computer tool. Those aim to support studies concerned with system-level simulations, damage fragility/loss assessment, and performance-based design.

CRediT authorship contribution statement

Ahmed Elkady: Writing – review & editing, Supervision, Software, Methodology, Conceptualization. **Zizhou Ding:** Writing – original draft, Visualization, Validation, Investigation, Data curation.

Declaration of Competing Interest

The authors declare that they have no known competing financial interests or personal relationships that could have appeared to influence the work reported in this paper.

Acknowledgments

This work was conducted at the National Infrastructure Laboratory, University of Southampton (UoS). The authors gratefully acknowledge the financial support provided by UoS to the first author as part of his studentship. The authors also acknowledge the use of the IRIDIS High Performance Computing Facility, and associated support services at the University of Southampton, in the completion of this work.

Appendix A. Supporting information

Supplementary data associated with this article can be found in the online version at doi:10.1016/j.engstruct.2025.121709.

Data availability

Some or all data, models, or code that support the findings of this study are available from the corresponding author upon reasonable request.

References

[1] AISC. Specifications for structural steel buildings†. ANSI/AISC 360-22. Chicago, †IL: American Institute for Steel Construction; 2022.
[2] CEN. Eurocode 3 - Design of Steel Structures, Part 1-8: Design of Joints. BS-EN 1993-1-8-2006. Brussels, Belgium: European Committee for Standardization; 2005.
[3] Lignos DG, Krawinkler H. Deterioration modeling of steel components in support of collapse prediction of steel moment frames under earthquake loading. J Struct Eng 2011;137(11). https://doi.org/10.1061/(ASCE)ST.1943-541X.0000376.
[4] Ibarra LF, Medina RA, Krawinkler H. Hysteretic models that incorporate strength and stiffness deterioration. Earthq Eng Struct Dyn 2005;34(12). https://doi.org/10.1002/eqe.495.
[5] Ding Z, Elkady A. Backbone moment-rotation models for partial-strength steel endplate connections. Eng Struct 2025 (accepted).
[6] Xu H, Ding Z, Elkady A. Traditional and machine-learning numerical models for partial-strength extended endplate connections. Proc 11th Int Conf Behav Steel Struct Seism Areas 2024. https://doi.org/10.1007/978-3-031-62884-9_47 (STESSA 2024), Salenro, Italy.
[7] Eatherton M.R., Nguyen T.N., Murray T.M., Yield line patterns for end-plate moment connections. Report No. CE/VPI-ST-21/05: Virginia Polytechnic Institute and State University, Blacksburg, VA, USA. 2021.
[8] Ding Z, Elkady A. Semirigid bolted end-plate moment connections: Review and experimental-based assessment of available predictive models. J Struct Eng 2023;149(9). https://doi.org/10.1061/JSENDH.STENG-11797.
[9] Landolfo R., D'Aniello M., Tartaglia R., Constanzo S., Demonceau J.-F., Jaspart J.-P., , EQUALJOINTS PLUS-Volume with pre-normative design recommendations for seismically qualified steel joints. No EQJ2-EN, Coimbra, Portugal. 2018.
[10] AISC. Seismic Provisions for Structural Steel Buildings. ANSI/AISC 341-22. Chicago, †IL: American Institute for Steel Construction; 2022.
[11] Elkady A, Ghimire S, Lignos DG. Fragility curves for wide-flange steel columns and implications on building-specific earthquake-induced loss assessment. Earthq Spectra 2018;34(3). https://doi.org/10.1193/122017eqs260m.
[12] Kukla D, Kozlowski A, Miller B, Ziaja D, Nykiel D. Experimental investigation of steel beam-to-column end-plate joints under static and impact loading. J Constr Steel Res 2024;212. https://doi.org/10.1016/j.jcsr.2023.108241.
[13] Kozłowski A, Kukla D. Experimental tests of steel unstiffened double side joints with flush and extended end plate. Arch Civ Eng 2019;65(4). https://doi.org/10.2478/ace-2019-0051.
[14] Skiadopoulos A, Lignos DG. Seismic demands of steel moment resisting frames with inelastic beam-to-column web panel zones. Earthq Eng Struct Dyn 2022;51(7). https://doi.org/10.1002/eqe.3629.
[15] Krawinkler H, Mohasseb S. Effects of panel zone deformations on seismic response. J Constr Steel Res 1987;8. https://doi.org/10.1016/0143-974X(87)90060-5.
[16] ABAQUS-FEA/CAE. Dassault Systemes Simulia Corp., RI, USA. © Dassault Systèmes, 2010, 2011.
[17] Hartloper AR, de Castro e Sousa A, Lignos DG. Constitutive modeling of structural steels: nonlinear isotropic/kinematic hardening material model and its calibration. J Struct Eng 2021;147(4). https://doi.org/10.1061/(ASCE)ST.1943-541X.0002964.
[18] Elkady A, Lignos DG. Improved seismic design and nonlinear modeling recommendations for wide-flange steel columns. ASCE J Struct Eng 2018;144(9). https://doi.org/10.1061/(ASCE)ST.1943-541X.0002166.
[19] Shi G, Shi Y, Wang Y. Behaviour of end-plate moment connections under earthquake loading. Eng Struct 2007;29(5). https://doi.org/10.1016/j.engstruct.2006.06.016.
[20] Gao JD, Yuan HX, Du XX, Hu XB, Theofanous M. Structural behaviour of stainless steel double extended end-plate beam-to-column joints under monotonic loading. Thin-Walled Struct 2020;151. https://doi.org/10.1016/j.tws.2020.106743.
[21] Zheng B, Wu D, Wang J, Shu G. Test on seismic behaviors of stainless steel bolted extended end-plate beam-column joints. Thin-Walled Struct 2024;196. https://doi.org/10.1016/j.tws.2023.111516.
[22] Tartaglia R, D'Aniello M, Rassati GA. Proposal of AISC-compliant seismic design criteria for ductile partially-restrained end-plate bolted joints. J Constr Steel Res 2019;159. https://doi.org/10.1016/j.jcsr.2019.05.006.
[23] AISC. Prequalified connections for special and intermediate steel moment frames for seismic applications. ANSI/AISC 358-16. Chicago, †IL: American Institute for Steel Construction; 2016.
[24] Breiman L, Friedman J, Olshen RA, Stone CJ. Classification and regression trees. Chapman and Hall/CRC; 2017.
[25] Breiman L. Bagging predictors. Mach Learn 1996;24(2). https://doi.org/10.1007/BF00058655.
[26] The MathWorks I. Statistics and Machine Learning Toolbox. Natick, Massachusetts: The MathWorks Inc; 2022. ⟨https://www.mathworks.com⟩.
[27] Chawla NV, Bowyer KW, Hall LO, Kegelmeyer WP. SMOTE: synthetic minority over-sampling technique. J Artif Intell Res 2002;16. https://doi.org/10.1613/jair.953.
[28] Bishop CM, Nasrabadi NM. Pattern recognition and machine learning. New York, NY: Springer; 2006.
[29] Lundberg SM, Lee S-I. A unified approach to interpreting model predictions. Proc 31st Conf Adv Neural Info Process Syst (NIPS 2017) 2017 (Long Beach, CA, USA).
[30] McKenna F. OpenSees: A framework for earthquake engineering simulation. Comput Sci Eng 2011;13(4). https://doi.org/10.1109/MCSE.2011.66.
[31] Gupta A, Krawinkler H. Behavior of ductile SMRFs at various seismic hazard levels. J Struct Eng 2000;126(1). https://doi.org/10.1061/(ASCE)0733-9445(2000)126:1(98).
[32] Skiadopoulos A, Elkady A, Lignos DG. Proposed panel zone model for seismic design of steel moment-resisting frames. J Struct Eng 2021;147(4). https://doi.org/10.1061/(ASCE)ST.1943-541X.0002935.
[33] Elkady A, Lignos DG. Modeling of the composite action in fully restrained beam-to-column connections: †Implications in the seismic design and collapse capacity of steel special moment frames. Earthq Eng Struct Dyn 2014;43(13). https://doi.org/10.1002/eqe.2430.
[34] Lin T, Wang Z, Hu F, Wang P. Finite-Element Analysis of High-Strength Steel Extended End-Plate Connections under Cyclic Loading. Materials 2022;15(8).
[35] Zoetemeijer P, Munter H. Influence of an axial load in the column on the behaviour of an unstiffened beam to column end plate connection. Stevin Laboratory Report No 6-84-1. Deft, Netherlands: Delft University of Technology; 1984.
[36] Zhu C, Rasmussen KJR, Yan S, Zhang H. Experimental full-range behavior assessment of bolted moment end-plate connections. J Struct Eng 2019;145(8). https://doi.org/10.1061/(ASCE)ST.1943-541X.0002368.
[37] Bu Y, Wang Y, Zhao Y. Study of stainless steel bolted extended end-plate joints under seismic loading. ThinWalled Struct 2019;144. https://doi.org/10.1016/j.tws.2019.106255.
[38] Elkady A. EEPC Classification App. United Kingdom: GitHub; 2025. ⟨https://github.com/amaelkady/SRConED/tree/main/EEPC_Classification_Model⟩.